The Astrophysical Journal, 623:291–301, 2005 April 10

DISCOVERY OF EXTREMELY EMBEDDED X-RAY SOURCES IN THE R CORONAE AUSTRALIS STAR-FORMING CORE

Kenji Hamaguchi,[1] Michael F. Corcoran,[2] Rob Petre, and Nicholas E. White
Exploration of the Universe Division, NASA Goddard Space Flight Center, Greenbelt, MD 20771; kenji@milkyway.gsfc.nasa.gov, corcoran@lheapop.gsfc.nasa.gov, robert.petre-1@nasa.gov, nwhite@lheapop.gsfc.nasa.gov

Beate Stelzer
INAF, Osservatorio Astronomico di Palermo, Piazza del Parlamento 1, I-90134 Palermo, Italy; stelzer@astropa.unipa.it

Ko Nedachi and Naoto Kobayashi
Institute of Astronomy, University of Tokyo, 2-21-1 Osawa, Mitaka, Tokyo 181-0015, Japan; nedachi@subaru.naoj.org, naoto@ioa.s.u-tokyo.ac.jp

and

Alan T. Tokunaga
Institute for Astronomy, University of Hawaii, 2680 Woodlawn Drive, Honolulu, HI 96822; tokunaga@ifa.hawaii.edu
Received 2004 June 16; accepted 2004 December 17

ABSTRACT

With the *XMM-Newton* and *Chandra* observatories, we detected two extremely embedded X-ray sources in the R Corona Australis (R CrA) star-forming core, near IRS 7. These sources, designated as X_E and X_W, have X-ray absorption columns of $\sim 3 \times 10^{23}$ cm^{-2} equivalent to $A_V \sim 180$ mag. They are associated with the VLA centimeter radio sources 10E and 10W, respectively; X_W is the counterpart of the near-infrared source IRS 7, whereas X_E has no *K*-band counterpart above 19.4 mag. This indicates that X_E is younger than typical Class I protostars, probably a Class 0 protostar, or in an intermediate phase between Class 0 and Class I. The X-ray luminosity of X_E varied between $29 < \log L_X < 31.2$ ergs s^{-1} on timescales of 3–30 months; X_E also showed a monotonic increase in X-ray brightness by a factor of 2 in 30 ks during an *XMM-Newton* observation. The *XMM-Newton* spectra indicate emission from a hot plasma with $kT \sim 3-4$ keV and also show fluorescent emission from cold iron. Although the X-ray spectrum from X_E is similar to flare spectra from Class I protostars in luminosity and temperature, the light curve does not resemble the light curves of magnetically generated X-ray flares, because the variability timescale of X_E is too long and variations in X-ray count rate were not accompanied by variations in spectral hardness. The short-term variation of X_E may be caused by the partial blocking of the X-ray plasma, while the month-long flux enhancement may be driven by mass accretion.

Subject headings: stars: activity — stars: magnetic fields — stars: pre–main-sequence — stars: rotation — X-rays: stars

1. INTRODUCTION

Low-mass protostars are divided into two classes, Class 0 and Class I, according to their infrared (IR) and radio spectral energy distribution (SED). This classification generally traces their evolutionary status. Class 0 objects are thought to be young ($t \sim 10^4$ yr) protostars, which mainly emit in the far-IR and submillimeter wavelengths with blackbody temperatures of <30 K (André et al. 1993). They are believed to be accreting mass dynamically from their huge circumstellar envelopes. Class I objects are believed to be older protostars ($t \sim 10^5$ yr) at the end of the mass accretion phase and emit in the near-IR at temperatures of $T \sim 3000-5000$ K.

Protostellar cores are generally hidden inside enormous gas envelopes. Hard X-rays can penetrate the thick molecular clouds, and hard X-ray observations have revealed high-energy activity associated with Class I objects (Koyama et al. 1996; Grosso et al. 1997; Imanishi et al. 2001). The observed X-ray emission exhibits occasional rapid outbursts reminiscent of solar flares, although current star formation theories do not predict solar-type magnetic dynamos in very young stars. Montmerle et al. (2000) proposed an alternative dynamo mechanism, in which fossil magnetic fields link the protostellar core with its circumstellar disk reconnect.

Hard X-ray emission from other embedded sources was reported in the OMC-2/3 cloud (Tsuboi et al. 2001). The two detected sources show Class 0 characteristics: huge absorption [$N_H \sim (1–3) \times 10^{23}$ cm^{-2}], no near-IR counterparts, and associations with millimeter radio clumps. However, follow-up radio and near-IR observations by Tsujimoto et al. (2004) did not unambiguously classify them as Class 0 protostars. In particular, one of these sources correlates with a centimeter radio source and a jet feature in the H_2 band, which indicates excitation by a jet from a nearby Class I protostar. Although Skinner et al. (2003) and Rho et al. (2004) have reported X-ray emission from other millimeter radio clumps in NGC 2024 and the Trifid Nebula, the photon statistics in those observations were too limited ($\lesssim 50$ photons per source) to identify their nature conclusively. To date no X-ray source has been clearly identified with a bona fide Class 0 object.

The R Corona Australis (R CrA) Cloud is a nearby star-forming region ($d \sim 170$ pc; Knude & Høg 1998). Among the many young stellar objects in the cloud, those in the IRS 7 region have attracted particular interest as a site of ongoing star

[1] Also at National Research Council, 500 Fifth Street, NW, Washington, DC 20001.
[2] Also at Universities Space Research Association, 7501 Forbes Boulevard, Suite 206, Seabrook, MD 20706.

TABLE 1
Observation Logs

Observation	Observatory	Sequence ID	Date	Exposure (ks)	Δ_{axis} (arcmin)	Shift ($\Delta\alpha$, $\Delta\delta$) (arcsec)
$Obs_{XMM\,1}$	*XMM-Newton*	146390101	2003 Mar 28	14.9/21.5	6	(0.4, −1.0)
$Obs_{XMM\,2}$	*XMM-Newton*	146390201	2003 Mar 29	18.1/24.0	6	(0.2, −1.3)
$Obs_{CXO\,1}$	*Chandra*	200017	2000 Oct 7	19.7	2	(0.03, 0.23)
$Obs_{CXO\,2}$	*Chandra*	200194	2003 Jun 26	37.6	0.2	(0.42, −0.03)

Notes.—Exposure: EPIC pn/MOS for *XMM-Newton*; Δ_{axis}: Off-axis angle of the IRS 7 region. Objects used for the position correction: IRS 2, IRS 5, HBC 677, CrA 1, ISO-CrA 136, HH 101 IRS 4, ISO-CrA 137, TY CrA, and HD 176386. IRS 1 and ISO-CrA 134 were also used for the position correction of the *Chandra* data.

formation. The region contains double-peaked, strong centimeter emission; an eastern peak is designated as 10E or IRS 7B, and a western peak is designated as 10W or IRS 7A (Brown 1987; Feigelson et al. 1998; Harju et al. 2001). It also contains two submillimeter peaks (van den Ancker 1999), multiple millimeter continuum peaks (Henning et al. 1994; Saraceno et al. 1996; Chini et al. 2003; Choi & Tatematsu 2004), and a signature of strong bipolar outflows (Harju et al. 1993; Anderson et al. 1997), but only one near-IR source, IRS 7 (Wilking et al. 1997, hereafter W97). These characteristics make the IRS 7 region a promising host of Class 0 sources. Koyama et al. (1996) detected hard X-ray emission and an intense flare from the IRS 7 region, which suggested the presence of a magnetically active protostar.

In this paper, we report the X-ray detection of two extremely embedded sources in the IRS 7 star-forming core during *XMM-Newton* observations in 2003. These results, combined with the analysis of two *Chandra* observations carried out in 2000 and 2003, and follow-up near-IR observations with the University of Hawaii 88 inch telescope (UH88), help to determine the nature of the detected X-ray sources.

2. X-RAY OBSERVATIONS AND ABSOLUTE POSITION CORRECTION

We analyzed X-ray data obtained with *XMM-Newton* on 2003 March 28 and 29 (hereafter $Obs_{XMM\,1}$ and $Obs_{XMM\,2}$; see Table 1 for details). *XMM-Newton* (Jansen et al. 2001) is composed of three nested Wolter I–type X-ray telescopes (Aschenbach et al. 2000) with European Photon Imaging Camera (EPIC) CCD detectors in their focal planes (Strüder et al. 2001; Turner et al. 2001). The observations were obtained with the EPIC pn and EPIC MOS1 and EPIC MOS2 detectors, in full-frame mode with the medium filter. We pointed at similar sky positions in $Obs_{XMM\,1}$ and $Obs_{XMM\,2}$; the IRS 7 star-forming core was at 6′ off-axis, where the 90% photon radius is ∼1′. We analyzed the X-ray data using the software package SAS, version 5.4.1, and HEAsoft, version 5.2. We first processed the data using the SAS scripts *emchain* and *epchain*, and screened out high background periods using standard criteria, excluding events when the entire chip count rate of "pattern = 0" events above 10 keV was >0.35 counts s^{-1} for MOS and >1 counts s^{-1} for pn, and excluding events close to hot pixels or outside the field of view. Finally, we selected events with pattern ≦ 4 for spectral analysis of the EPIC pn and with pattern ≦12 for the EPIC MOS and the other analyses of the EPIC pn.

To help source identification and investigate long-term flux variations, we analyzed two archival *Chandra* observations. *Chandra* has a single high-performance X-ray telescope that provides subarcsecond imaging (Weisskopf et al. 2002). The *Chandra* observations were obtained using the Advanced CCD Imaging Spectrometer detector using the Imaging array (ACIS-I) on 2000 October 7 and 2003 June 26 (hereafter $Obs_{CXO\,1}$ and $Obs_{CXO\,2}$; see Table 1). Garmire & Garmire (2002) presented the first results of $Obs_{CXO\,1}$. The IRS 7 star-forming region was at 2′ and 0.′2 off-axis in $Obs_{CXO\,1}$ and $Obs_{CXO\,2}$, respectively, where the 90% photon radius is ∼1″. We analyzed the *Chandra* data using the software packages CIAO, version 2.3, and HEAsoft, version 5.2. For $Obs_{CXO\,1}$, we reprocessed the level 1 event data with *acis_process_events* to compensate for degradation of the CCD spectral resolution by charge transfer inefficiency (CTI; Townsley et al. 2000). For $Obs_{CXO\,2}$, we used pipeline-processed level 2 event data that were already corrected for CTI degradation. Finally, we selected events from both observations with the standard grades 0, 2, 3, 4, and 6 in the *ASCA* event grade system for further analysis.

For the correction of the absolute coordinates, we measured positions of X-ray–bright sources on the combined EPIC pn + MOS images between 0.3 and 10 keV and positions of sources in the ACIS-I image between 0.5 and 9 keV using available source detection packages (SAS, *edetect_chain*; CIAO, *wavdetect*; see also Table 1). We correlated these positions with near-IR source

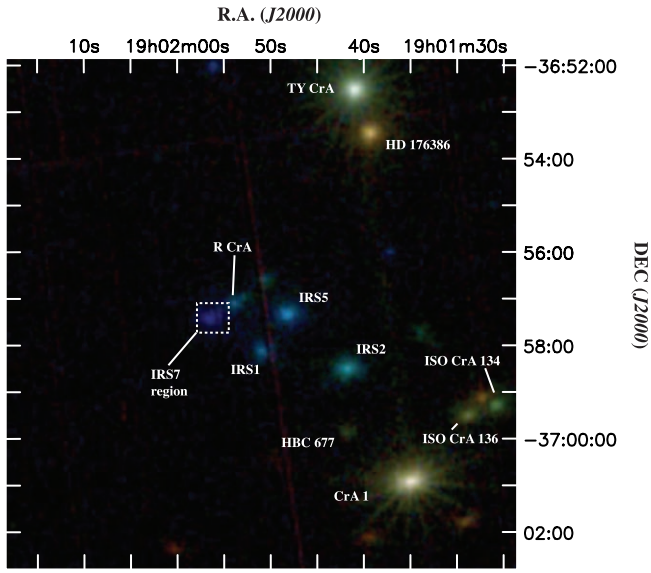

Fig. 1.—*XMM-Newton* true-color image of the R CrA star-forming region ($Obs_{XMM\,1}$ + $Obs_{XMM\,2}$). The image is color coded to represent hard band (3–9 keV) to blue, medium band (1–3 keV) to green, and soft band (0.2–1 keV) to red. The dotted rectangle shows the IRS 7 region (field of view of Fig. 2, except the bottom right panel). Class I protostar: IRS 1, IRS 2, IRS 5; Herbig Ae/Be star: R CrA, TY CrA, HD 176386; weak-lined T Tauri star: CrA 1.

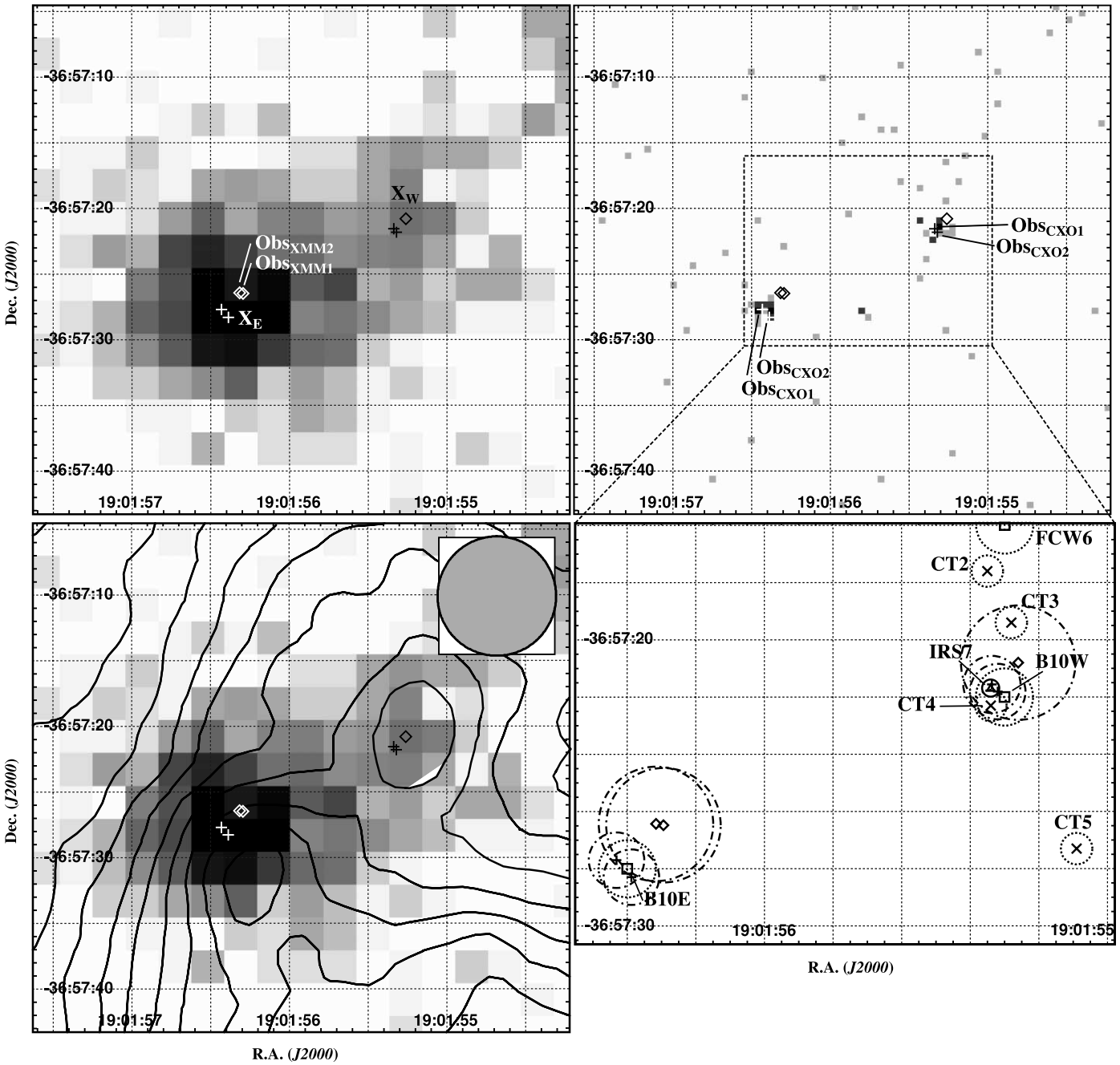

FIG. 2.—Magnified images of the IRS 7 region. *Top left*: 3–9 keV EPIC pn + MOS image of *XMM-Newton* combining $\mathrm{Obs}_{XMM\,1}$ and $\mathrm{Obs}_{XMM\,2}$. *Top right*: 0.5–9 keV image of *Chandra* in $\mathrm{Obs}_{CXO\,1}$. *Bottom left*: *XMM-Newton* image overlaying flux contours in submillimeter at 450 μm taken by van den Ancker (1999). *Bottom right*: Source positions with their error circles including sources in near-IR and radio wavelengths. Diamonds show *XMM-Newton* sources, plus signs show *Chandra* sources, squares show centimeter radio sources (B number, Brown 1987; FCW number, Feigelson et al. 1998; source positions are referred to Feigelson et al. 1998), crosses show millimeter radio sources (CT number; Choi & Tatematsu 2004), and triangle shows near-IR source (IRS 7). The gray circle (*bottom left*) shows the beam size of the submillimeter telescope. Error circles (*bottom right*) are drawn in a dot-dashed line for X-ray sources, a dotted line for radio sources, and a solid line for the near-IR source IRS 7.

positions in the 2MASS All-Sky Point Source Catalog (PSC) obtained from the NASA/IPAC Infrared Science Archive (GATOR),[3] whose astrometric accuracy is good to about 0.″1.[4] Each X-ray source has only one 2MASS counterpart within 4″, so that the source identification is very reliable. After adjusting the X-ray positions to the 2MASS positions, the deviation of the *Chandra* and *XMM-Newton* coordinates from the 2MASS coordinates is $\lesssim$0.″6.

3. X-RAY IMAGE

Figure 1 shows a "true-color" X-ray image of the R CrA star-forming region, which combines EPIC pn and MOS (1 + 2) data taken in both $\mathrm{Obs}_{XMM\,1}$ and $\mathrm{Obs}_{XMM\,2}$. Red, green, and blue colors in the image represent soft (0.2–1 keV), medium (1–3 keV), and hard (3–9 keV) bands, respectively. The IRS 7 region is colored in dark blue, which indicates the presence of

[3] See http://irsa.ipac.caltech.edu/applications/Gator.

[4] See § 2.2 of Explanatory Supplement to the 2MASS All-Sky Data Release at http://www.ipac.caltech.edu/2mass/releases/allsky/doc/explsup.html.

TABLE 2
DETECTED SOURCES

Source	Designation	Observation	α (J2000.0), δ (J2000.0)[a]	Net Counts	K-Band (mag)	Counterpart
X_E.....	XMMU J190156.3−365726	$Obs_{XMM\,1}$	19 1 56.29, −36 57 26.5	467.7	≳19.4	10E[b], vdA 5(?)[c]
		$Obs_{XMM\,2}$	19 1 56.32, −36 57 26.4	1611.3	...	...
	CXOU J190156.4−365728	$Obs_{CXO\,1}$	19 1 56.43, −36 57 27.7	19.6	...	...
		$Obs_{CXO\,2}$	19 1 56.39, −36 57 28.3	12.7	...	...
X_W.....	XMMU J190155.3−365721	$Obs_{XMM\,1}$ and $Obs_{XMM\,2}$	19 1 55.26, −36 57 20.8	114.0[d]	12.2[e]	10W[b], Source 4[f], IRS 7, vdA 3(?)[c]
	CXOU J190155.3−365722	$Obs_{CXO\,1}$	19 1 55.34, −36 57 21.6	12.7	...	...
		$Obs_{CXO\,2}$	19 1 55.32, −36 57 21.8	22.4	...	...

NOTES.—Units of right ascension are hours, minutes, and seconds, and units of declination are degrees, arcminutes, and arcseconds. Net counts: EPIC pn + MOS for *XMM-Newton*.

[a] Positional uncertainties are $\sim 2''$ for *XMM-Newton* and $\sim 1''$ for *Chandra*.
[b] Reference to Brown (1987) and Feigelson et al. (1998).
[c] Reference to van den Ancker (1999).
[d] Net counts in $Obs_{XMM\,1}$.
[e] Reference of the K' magnitude of R1 (IRS 7) to Wilking et al. (1997).
[f] Reference to Choi & Tatematsu (2004).

hard X-ray sources, possibly suffering from strong low-energy absorption. The top left panel of Figure 2 shows a detailed view of the IRS 7 region of the hard-band image. A strong X-ray source, labeled X_E, was detected with *edetect_chain* in both $Obs_{XMM\,1}$ and $Obs_{XMM\,2}$ (Table 2). Although *edetect_chain* failed to detect a small peak on the tail of the point-spread function to the northwest of X_E, our subsequent analysis using the $Obs_{XMM\,1}$ data confirmed it as a weak source at ~ 14 σ significance, which we labeled X_W. The positional accuracy of both sources is hard to estimate because the sources are unresolved. In this paper, we tentatively put the errors at $\sim 2''$, the half-pixel size of the EPIC pn camera. If we rely on the result of *edetect_chain*, the absolute position accuracy of X_E is $1''.7$ for $Obs_{XMM\,1}$ and $1''.2$ for $Obs_{XMM\,2}$ at 90% confidence.

Chandra detected two weak X-ray sources in the IRS 7 region at above 4 σ significance in both $Obs_{CXO\,1}$ and $Obs_{CXO\,2}$ (top right panel of Fig. 2 for $Obs_{CXO\,1}$; Table 2). Although each source has less than 20 photons, the absolute source positions are determined within $1''$, thanks to the excellent spatial resolution of *Chandra*. These detected sources have corresponding *XMM-Newton* sources, although, if we take the error circles derived using the *edetect_chain* results, the source positions of X_E between the *Chandra* and *XMM-Newton* observations have a significant discrepancy of $\sim 2''$. Hereafter, we refer to the *Chandra* detected positions for both sources.

The bottom panels of Figure 2 compare the X-ray source positions with sources detected at other wavelengths; X_E is associated with the VLA centimeter source 10E (Brown 1987) and the submillimeter peak vdA 5 (van den Ancker 1999). Choi & Tatematsu (2004) also suggested a marginal millimeter source at the position of X_E; X_W is associated with centimeter (10W in Brown 1987), millimeter (source 4 in Choi & Tatematsu 2004), and submillimeter sources, and the near-IR source, IRS 7 (see also § 5).

4. X-RAY LIGHT CURVES AND SPECTRA

4.1. *East Source* (X_E)

We extracted source photons from the *XMM-Newton* observations of X_E from a $27''.5$ radius circle centered on the source position excluding the region around X_W, with background taken from appropriate source-free regions. We obtained ~ 2000 net counts from $Obs_{XMM\,1}$ and $Obs_{XMM\,2}$, enabling us to perform detailed timing and spectral analyses. For the *Chandra* data, we extracted events from a $1''.8$ radius circle centered on the source position. The background level was negligibly low. Only 10–20 counts were extracted from the *Chandra* observation, which precludes detailed spectral analysis.

The top panel of Figure 3 shows the background subtracted EPIC pn + MOS light curve of X_E in the 2–10 keV band. The first half of the light curve, corresponding to $Obs_{XMM\,1}$, is mostly flat with some indications of a slight increase at the end. A constant provides an acceptable χ^2 fit at above 90% confidence (Table 3). The source was about 4 times brighter than the average count rate of $Obs_{XMM\,1}$ at the beginning of the second half, corresponding to $Obs_{XMM\,2}$, and the count rate gradually

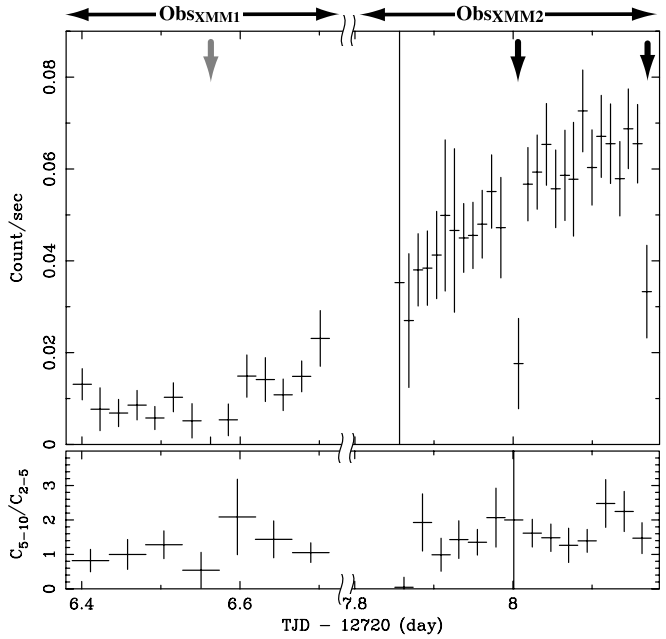

FIG. 3.—Light curve of X_E in the 2–10 keV band (*top*) and the hardness ratio defined as "count rates in the 5–10 keV band/count rates in the 2–5 keV band" (*bottom*). Points with error bars in the top and bottom panels are made from summed data sets of EPIC pn + MOS (1 + 2). The horizontal axis is truncated Julian day (TJD) −12,720. The arrows show timings of the dip feature. Bins in the top panel have 2 ks for $Obs_{XMM\,1}$ and 1 ks for $Obs_{XMM\,2}$, and bins in the bottom panel have 4 ks for $Obs_{XMM\,1}$ and 2 ks for $Obs_{XMM\,2}$.

TABLE 3
FITTING RESULT OF THE X_E LIGHT CURVE

Observation	Binning (s)	Model	Constant (10^{-2} counts s^{-1})	Linear (10^{-2} counts s^{-1} day^{-1})	χ^2/dof (dof)
$Obs_{XMM\,1}$	2000	Constant	0.93	...	1.63 (13)
$Obs_{XMM\,2}$	1000	Constant	5.3	...	1.96 (26)
	1000	Constant + linear	3.7[a]	9.3	1.21 (25)

[a] Count rate at TJD = 12,727.8564 days.

increased by a factor of 2. This part of the light curve can be acceptably fitted at greater than 90% confidence level by a linear increase with a slope of $\sim 9.3 \times 10^{-2}$ counts s^{-1} day^{-1} (Table 3). During both observations, the hardness ratio defined as count rates in the 5–10 keV band over those in the 2–5 keV band remained unchanged, except for a minimum at 7.86 days. This means that time variation in the count rate was not accompanied by any significant change of the spectral shape. On the other hand, the light curves show marginal dips on timescales of <1 ks near 8.02 and 8.17 days. These dips are seen in both the pn and MOS light curves of X_E, and other nearby sources, such as R CrA, IRS 5, and CrA 1, have no dips at those times. These facts do not support an instrumental origin. We note that these dips might suggest a tentative period of $\sim$13.9 ks, with the combination of minimal dips at 6.56 and 7.85 days (the dip at 7.85 day was only covered with the MOS data and does not appear in Fig. 3).

The EPIC spectra of X_E in $Obs_{XMM\,1}$ and $Obs_{XMM\,2}$ (Fig. 4) show several similarities: significant emission up to $\sim$10 keV, strong absorption below 2–3 keV, a broad-line feature between 6 and 7 keV, and marginal lines between 5 and 6 keV in the EPIC pn spectra (which may be of instrumental or cosmic origin).[5] To investigate the 6–7 keV line feature, we fitted the EPIC pn and MOS (1 + 2) spectra simultaneously with an absorbed power-law model with a Gaussian component. An acceptable fit above 90% confidence has a photon index of 3.0 (2.5–3.4), a Gaussian line centroid of 6.60 (6.53–6.67) keV, and a Gaussian width of 0.15 (0.079–0.28) keV, where the numbers in parentheses denote the 90% confidence range. The derived Gaussian width, equivalent to $\Delta v \sim 7000$ km s^{-1} if produced by Doppler broadening, is unreasonably large for a stellar plasma (see also § 6.1). We therefore interpret the broad feature as a blend of iron lines from a hot plasma at 6.7 keV and a fluorescent iron line at 6.4 keV, although the profile needs to be confirmed with deeper observations. We then fitted the *XMM-Newton* spectra with XSPEC by an absorbed 1-temperature (1T), optically thin, thermal plasma model (WABS, Morrison & McCammon 1983; MEKAL, Mewe et al. 1995) with a Gaussian component with line center fixed at 6.4 keV. For either of the two observations this model yields acceptable fits at the 90% confidence level (models A and B in Table 4); N_H differs significantly between $Obs_{XMM\,1}$ and $Obs_{XMM\,2}$, possibly because of the simplistic spectral model we assumed. Indeed, the soft emission below 3 keV was unchanged between $Obs_{XMM\,1}$ and $Obs_{XMM\,2}$, suggesting an additional component along with the hard emission. In the single-temperature fit to $Obs_{XMM\,1}$, the soft emission is included as a part of the absorption slope, whereas the fit to $Obs_{XMM\,2}$ determines N_H from the 3–5 keV slope and does not reflect the soft emission.

[5] See § 3.3.7.2 in *XMM-Newton* Users' Handbook at http://xmm.vilspa.esa.es/external/xmm_user_support/documentation/uhb/index.html.

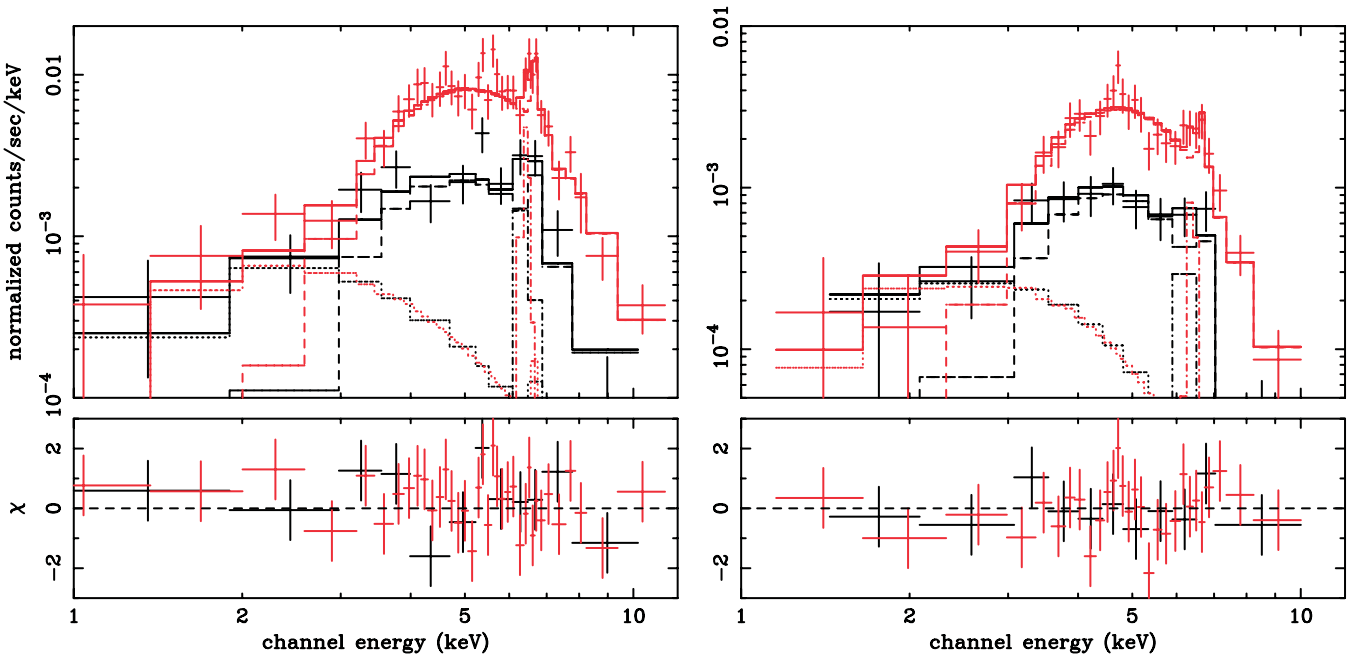

FIG. 4.—EPIC pn (*left*) and MOS (1 + 2) (*right*) spectra of X_E in $Obs_{XMM\,1}$ (*black*) and $Obs_{XMM\,2}$ (*red*). The solid lines show the best-fit model of the simultaneous fitting with EPIC pn and MOS. Dotted lines show the soft component, the dashed line shows the hard component, and dot-dashed lines show the Gaussian component for the line at 6.4 keV. Each bottom panel shows the residuals of the χ^2 fit.

TABLE 4

FITTING RESULTS OF THE SPECTRA

Source	Observation	Model	Component	$N_{\rm H}$ (10^{22}cm^{-2})	kT (keV)	Abundance (solar)	log EM (cm^{-3})	Flux$_{6.4\ \rm keV}$ (10^{-6} counts cm^{-2} s^{-1})	χ^2/dof (dof)	log $L_{\rm X}$ (ergs s^{-1})
X_E.....	Obs$_{XMM\,1}$	A (1T)	...	13.2 (9.6−18.3)	5.1 (2.8−10.4)	0.5 (0.2−1.4)	53.2 (53.0−53.6)	2.4	1.22 (21)	30.4
	Obs$_{XMM\,2}$	B (1T)	...	24.7 (21.6−28.3)	4.4 (3.4−6.1)	0.2 (0.1−0.3)	54.1 (54.0−54.1)	3.4	0.99 (66)	31.2
	Obs$_{XMM\,1}$ and Obs$_{XMM\,2}$	C (2T)	Var$_1$	28.1 (22.5−33.8)	2.7 (1.8−4.2)	0.2 (0.1−0.3)	53.8 (53.5−54.1)	2.8 (0.8−4.8)	0.97 (86)	30.8
	...	...	Var$_2$	= Var$_1$	4.0 (2.9−5.3)	= Var$_1$	54.1 (54.0−54.4)	3.4 (1.4−5.5)	...	31.2
	...	...	Const.	4.2 (1.4−11.4)	2.3 (0.4−)	= Var$_1$	52.5 (51.8−53.5)	...	...	29.6
X_W.....	Obs$_{XMM\,1}$	D (1T)	...	33.7 (19.1−60.0)	4.7 (1.6−)	0.3 (fix)	53.3 (52.8−54.3)	...	0.65 (8)	30.5
	Obs$_{CXO\,1}$ and Obs$_{CXO\,2}$	E (1T)	...	33.7 (fix)	4.7 (fix)	0.3 (fix)	52.9 (52.8−53.0)	...	0.60 (3)	30.0

NOTES.—Var$_{1(2)}$: variable hard component in Obs$_{XMM\,1}$ (Obs$_{XMM\,2}$). Const.: constant soft component; $L_{\rm X}$: absorption-corrected X-ray luminosity in the 0.5–10 keV band. Distance assumes $d \sim 170$ pc.

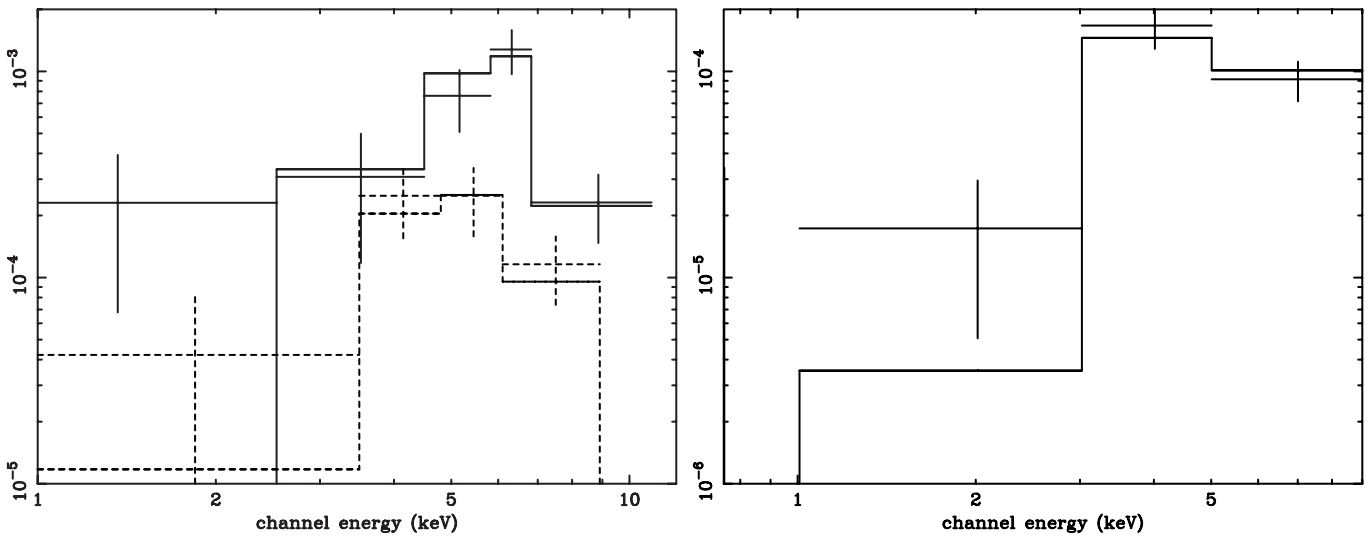

FIG. 5.—The X_W spectra in $Obs_{XMM\,1}$ (*left*: *solid line*, pn; *dotted line*, MOS) and $Obs_{CXO\,1}$ + $Obs_{CXO\,2}$ (*right*). Both panels show data points and their best-fit models (models D and E in Table 4 from left).

We therefore refitted the spectra of $Obs_{XMM\,1}$ and $Obs_{XMM\,2}$ simultaneously with an absorbed 2T model—1T for the variable hard component and 1T for the constant soft component—with a Gaussian line at 6.4 keV. In this model, we tied the N_H of the hard components in $Obs_{XMM\,1}$ and $Obs_{XMM\,2}$ and tied the elemental abundances of all components. We allowed N_H of the soft and hard components to be fitted independently, because a model fit with a common N_H gives large $N_H \sim 2.4 \times 10^{23}$ cm^{-2} and hence an unrealistically large intrinsic $\log L_X \sim 35$ ergs s^{-1} for the soft component. The model, again, successfully reproduced the spectra above the 90% confidence level (model C in Table 4). The derived physical parameters of the hard component are at the higher end among those of Class I protostars (e.g., see Imanishi et al. 2001 for comparison): large $N_H \sim 2.8 \times 10^{23}$ cm^{-2}, equivalent to $A_V \sim 180$ mag (using the N_H-A_V relation by Imanishi et al. 2001); plasma temperature of 3–4 keV; $\log L_X \sim 30.8$ ergs s^{-1} in $Obs_{XMM\,1}$, which further increased to $\sim$31.2 ergs s^{-1} in $Obs_{XMM\,2}$; and a fluorescent iron line equivalent width (EW) of $\sim$810 (240–1400) eV in $Obs_{XMM\,1}$ and $\sim$250 (100–400) eV in $Obs_{XMM\,2}$. Meanwhile, the metal abundance is $\sim$0.2 (0.1–0.3) solar, which is typical of low-mass young stars (e.g., Favata et al. 2003).

Since we have very few counts from the *Chandra* observations, we simply calculated a softness ratio, defined as $S/(H + S)$, where S and H are photon counts in the 0.5–3 and 3–9 keV bands, respectively. The ratios are 0.15 ± 0.08 ($S = 3, H = 17$) in $Obs_{CXO\,1}$ and 0.38 ± 0.13 ($S = 5, H = 8$) in $Obs_{CXO\,2}$, where the errors show 1 σ. The same softness ratios evaluated for the *XMM-Newton* best-fit models after adjusting to the *Chandra* ACIS-I response are 0.11 for $Obs_{XMM\,1}$ and 0.048 for $Obs_{XMM\,2}$, suggesting that the spectra have been softer during the *Chandra* observations. This is consistent with the picture that the hard component further declined during the *Chandra* observations while the soft component was unchanged.

4.2. *West Source* (X_W)

We extracted *XMM-Newton* source events of X_W from an ellipse with axes 15″ by 10.″5 elongated toward the north-northeast direction, excluding a region with strong contamination from X_E, and selected the background from a symmetrical region near X_E. We did not use the $Obs_{XMM\,2}$ data because the X_W region suffered strong contamination from X_E. For the *Chandra* data, we extracted source events from a 1.″8 radius circle. The background level was negligibly low.

The *XMM-Newton* spectra were reproduced by an absorbed 1T model with $N_H \sim 3.4 \times 10^{23}$ cm^{-2}, $kT > 1.6$ keV, and $\log L_X \sim 30.5$ ergs s^{-1} (left panel of Fig. 5; model D in Table 4). We added both spectra from $Obs_{CXO\,1}$ and $Obs_{CXO\,2}$ because their count rates are about the same. The summed spectrum can be reproduced by the best-fit *XMM-Newton* model just by changing its normalization (right panel of Fig. 5; model E in Table 4).

5. FOLLOW-UP OBSERVATIONS IN THE NEAR-IR

Infrared source catalogs in the R CrA region currently available have several shortcomings: shallow limiting magnitude (e.g., $K_{limit} \sim 15$ mag for 2MASS; 16.5 mag for W97), insufficient spatial resolution (e.g., 1″ pixel^{-1} for 2MASS and 0.″75 pixel^{-1} for W97), and insufficient positional accuracy (e.g., $\pm$1″ for W97). We therefore analyzed two deep *K*-band images of the field obtained in 1998 August and 2003 August using UH88 and the near-IR imager QUIRC. During the observations, we used the f/10 secondary mirror, yielding a pixel scale of 0.″1886 pixel^{-1}. The spatial resolution of our images is 0.″5 and 0.″8 in FWHM for the 1998 and 2003 data, respectively. Both images were aligned with an accuracy of 0.″3 by referring to the coordinates of R CrA in the 2MASS catalog and a high-resolution image (FWHM $\sim$ 0.″14) obtained with the Subaru Telescope. The analysis was made with IRAF.[6]

Both images show R CrA as a filamentary and mildly extended reflection nebulae (see Fig. 6 for the 1998 data), but the location of X_E shows no significant emission, although it does have some marginal enhancement. The flux upper limit was measured by subtracting the extended nebular emission, which we estimated with a third-order polynomial surface fit. The 5 σ upper limit of X_E within the 20×20 pixel box centered at X_E was $\sim$19.4 mag for the 1998 image and $\sim$19 mag for the 2003 image. Meanwhile, using the Subaru image (K. Nedachi et al. 2005, in preparation), we measured the absolute position of IRS 7

[6] IRAF is distributed by the National Optical Astronomy Observatory, which is operated by the Association of Universities for Research in Astronomy, Inc., under cooperative agreement with the National Science Foundation.

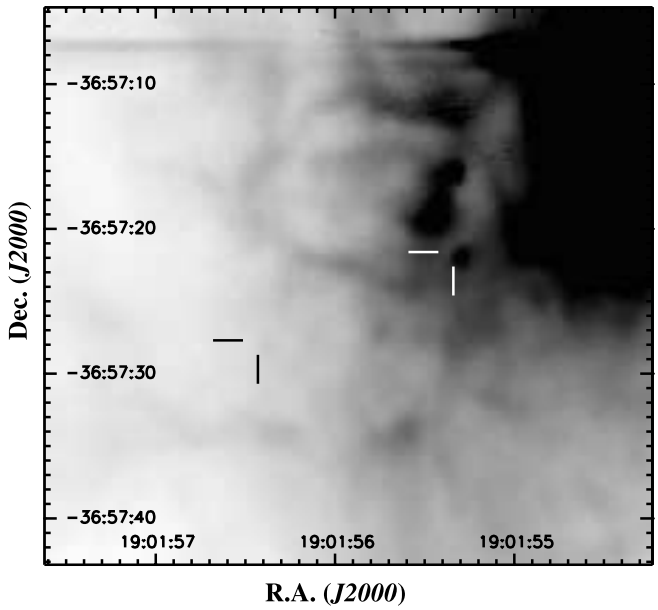

FIG. 6.—The *K*-band image of the IRS 7 region obtained in 1998. The X_E and X_W positions measured with *Chandra* are at the left and right crosses, respectively.

at (α [J2000.0], δ [J2000.0]) = ($19^h1^m55^s.34$, $-36°57'21''.69$) with an accuracy of $0''.3$. This is much more accurate than the earlier observations. With this new position, IRS 7 falls within the positional error circle of X_W (see the bottom right panel of Fig. 2).

6. DISCUSSION

6.1. *The Nature and X-Ray Emission Mechanism of* X_E

Harju et al. (2001) suggested that the radio counterpart of X_E, source 10E, might be a radio galaxy or Galactic microquasar. However, AGNs with the observed X-ray flux above $(2–8)\times10^{-13}$ ergs cm^{-2} s^{-1} (2–10 keV) are found $\lesssim$10 deg^{-2} in the sky (Ueda et al. 1998), and the probability of detecting such an active galactic nucleus (AGN) in the IRS 7 star-forming core ($\sim$10 arcsec^2) is extremely small ($\lesssim10^{-4}$). Furthermore, AGNs do not generally show thermal iron K emission line and have rather flat spectral slopes ($\Gamma \leq 2$; Ueda et al. 1998). Similarly, Galactic black hole candidates also show flat power-law X-ray spectra with $\Gamma = 1.5–2.1$, although they sometimes show thermal spectra with $kT \sim 0.5–1.5$ keV (McClintock & Remillard 2005). Taking its association to the star-forming core into account, X_E is most likely a very young stellar object.

Compared to Class I objects in R CrA star-forming region such as IRS 1, 2, and 5, which have $N_H \sim 2\times10^{22}$ cm^{-2} and $K \lesssim 11$ mag (from our additional analysis of the $Obs_{XMM\,1}$ and $Obs_{XMM\,2}$ data; see also W97), X_E shows much larger X-ray absorption and much smaller near-IR luminosity; X_E is also associated with the strong submillimeter condensation (vdA 5; van den Ancker 1999). All these suggest that X_E is much younger than typical Class I objects, and that it is a Class 0 object or an object in an intermediate phase between Class 0 and Class I. We note that extremely embedded sources in the OMC-2/3 cloud have similarly high absorption columns of $N_H \sim (1–3)\times10^{23}$ cm^{-2} (Tsuboi et al. 2001).

Between the *Chandra* and *XMM-Newton* observations, X_E exhibited strong long-term X-ray variation by a factor of 10–100 on a timescale of a month (Fig. 7). In none of the observations did we detect obvious flare activity, although $Obs_{XMM\,2}$ showed a marked flux increase. Active stars such as RS CVn and young stars in open clusters do not generally vary in X-rays by more than a factor of 2–3 outside flares (Stern 1998). Less active stars such as the Sun exhibit strong X-ray variations by up to a factor of 100, coincident with their activity cycles (e.g., Favata et al. 2004), but unlike X_E, the X-ray luminosity of such stars is typically less than 10^{28} ergs s^{-1} and the observed activity timescale is several years. One possibility is that the strong variability of X_E could indicate abrupt activity produced by an enhanced mass accretion episode similar to that recently attributed to the outburst of the star in McNeil's Nebula (Kastner et al. 2004). Indeed, the outburst increased the X-ray flux by a factor of 50, and the post-outburst X-ray luminosity of 10^{31} ergs s^{-1} is comparable to the luminosity of X_E during $Obs_{XMM\,2}$.

The plasma temperature and X-ray luminosity of X_E exceed the typical quiescent X-ray activity of Class I protostars and are comparable to temperatures and luminosities of X-ray

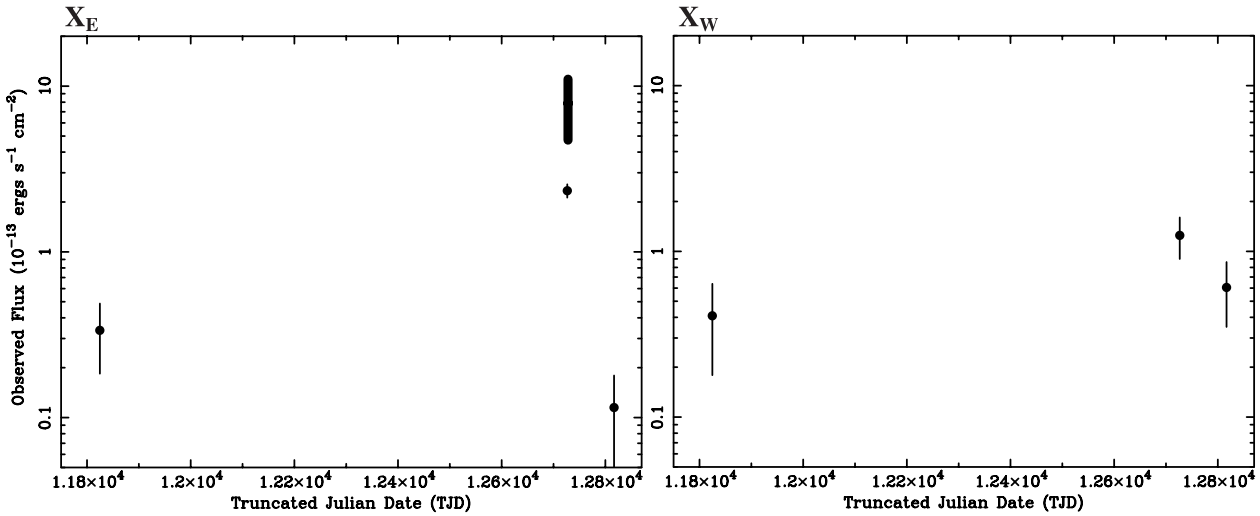

FIG. 7.—Observed X-ray flux between 0.5 and 10 keV in long timescale (*left*, X_E; *right*, X_W). The vertical narrow bars on the data points show photon statistical error at 90% confidence level. The thick bar shows the variable range of X_E during $Obs_{XMM\,2}$.

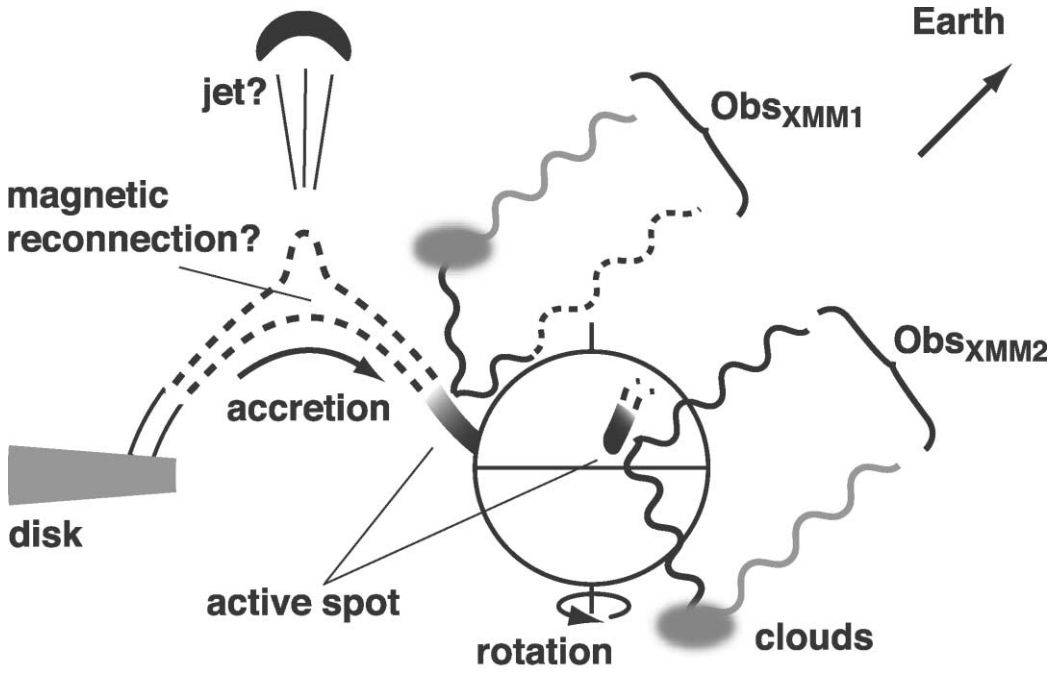

FIG. 8.—Possible geometry of the protostellar core, jet, and observer. The wavy lines show X-ray emission (*solid line*, direct X-rays; *gray line*, fluorescent and scattering X-rays; *dotted line*, direct X-rays are partially covered).

flares from Class I protostars (Imanishi et al. 2001; Shibata & Yokoyama 2002).[7] X-ray flares from Class I protostars may be produced by reconnection in a magnetosphere that is twisted because of the core-disk differential rotation (Tsuboi et al. 2000; Montmerle et al. 2000). Perhaps a similar mechanism explains the X-ray emission from X_E during the *XMM-Newton* observations, although magnetic reconnection would have to occur throughout the *XMM-Newton* observations since no rapid X-ray variation was seen from X_E.

The flux increase of a factor of 2 in $\sim$30 ks in Obs$_{XMM\,2}$ is unlike the types of variations seen in magnetically driven X-ray flares, which are characterized by rapid ($\sim$10 ks) flux increases (e.g., Tsuboi et al. 1998, 2000; Stelzer et al. 2000; Imanishi et al. 2001). Favata et al. (2003) found a similar rise in X-ray brightness in the classical T Tauri star XZ Tau, with a factor of 4 increase during 50 ks. In this case, the brightening was accompanied by an N_H decrease, and therefore Favata et al. (2003) interpreted it as an eclipse of the emitting region by the accretion stream. Because X_E did not show any significant hardness ratio variation, the absorber would have to be uniformly dense, optically thick gas. Such a variation could be produced by an eclipse of the X-ray–emitting region by an absorber or emergence of the X-ray–emitting region from behind the rim of the protostellar core as a result of stellar rotation.

If the fluorescent iron line in the spectra is real, then this is unusual because fluorescent iron lines have been rarely observed from pre–main-sequence stars. Even a few examples during strong flares from Class I protostars have EW $\lesssim$ 150 eV (Imanishi et al. 2001). The large EW of the fluorescent line from X_E ($\sim$250–800 eV) again suggests that the source is extremely embedded. When we simulate fluorescent iron line EWs, assuming solar abundance for the surrounding cold gas (Inoue 1985), an optically thick absorber should block the direct X-ray emission by $\sim$60% for Obs$_{XMM\,1}$ and $\sim$3% for Obs$_{XMM\,2}$. This result is consistent with obscuration of the X-ray emission, although the blocking factor in Obs$_{XMM\,2}$ should be $\gtrsim$30% to explain the observed flux increase in Obs$_{XMM\,2}$. Interestingly, the intrinsic X-ray luminosity in Obs$_{XMM\,1}$ should be $\log L_X \sim 31.2$ ergs s^{-1}, which is comparable to L_X in Obs$_{XMM\,2}$.

Our thermal model fit requires a metal abundance of $\sim$0.2 (0.1–0.3) solar. Although the derived abundance is dependent on the thermal model, and identifying emission lines in low-resolution spectroscopy may be difficult especially around $\sim$1 keV (e.g., Kastner et al. 2002), the metal abundance of X_E is determined mostly from the iron K line region, which seems to show a real underabundance. X-ray emission from T Tauri stars similarly show subsolar abundances (e.g., Favata et al. 2003). This might suggest that X_E has an X-ray emission mechanism similar to that of T Tauri stars. Such abundance anomalies could be produced by the first ionization potential (FIP) effect (e.g., Güdel et al. 2001). Unfortunately, the spectrum of X_E does not have enough counts to detect, unambiguously, emission lines from other elements such as argon and calcium to test the FIP effect. Another possible solution is that the continuum emission includes a nonthermal component, as proposed for ρ Oph S1 (Hamaguchi et al. 2003).

From the above discussion, we hypothesize that the X-ray plasma responsible for the hard component was produced at a mass accretion spot on the protostellar core. The X-ray emission is blocked when the spot would have been behind the protostellar core during Obs$_{XMM\,1}$, and just appeared from behind the rim in Obs$_{XMM\,2}$ as a consequence of protostellar

[7] Imanishi et al. (2001) used the distance to the ρ Oph cloud of 165 pc instead of 120 pc derived from more reliable *Hipparcos* data (Knude & Høg 1998) for a comparison to earlier X-ray results of the ρ Oph field. Their X-ray luminosity should be divided by a factor of 2 to compare to our results.

rotation (Fig. 8). To be consistent with the observed *XMM-Newton* light curves, the rotational period of the protostellar core would need to be $\gtrsim 2.8$ days. This rotation speed is much slower than the breakup rotation speculated for Class 0 protostars from rotational periods of Class I protostars (e.g., Montmerle et al. 2000).

The soft component was apparently constant and had much smaller N_H compared to the hard component. This may suggest that the component has no physical connection to, and exists far from, the hot component. One possible origin is that the soft component is associated with another hidden protostar, but although the N_H of the soft component is typical of Class I protostars, the *K*-band magnitude of $\gtrsim$19 mag is much larger than those of Class I protostars in the R CrA cloud ($K \lesssim 11$ mag). Another possible origin is that the X-ray plasma is heated by a collision of a steady jet or outflow from X_E with circumstellar gas, a mechanism thought to be associated with X-ray emission from HH 2, L1551 IRS 5, and OMC 2/3 (Pravdo et al. 2001; Favata et al. 2003; Tsujimoto et al. 2004). Indeed, X_E is associated with a centimeter radio source as those systems, but the plasma temperature and X-ray luminosity of X_E are very large compared to those sources, except for the source in OMC 2/3. Such a high plasma temperature requires an energetic jet with $v_{jet} \sim 1500$ km s^{-1}. While low-mass young stars generally have slow outflow velocities (a few hundred km s^{-1}), Marti et al. (1995) measured a large proper motion in the young stellar jets HH 80–81, implying velocities up to 1400 km s^{-1}; X_E could be another example of a source with high-speed outflow.

6.2. *What Is* X_W*?*

The source X_W is a counterpart to the near-IR source IRS 7 as well as the centimeter radio source 10W. The column density of X_W [$\sim(2\text{–}6)\times10^{23}$ cm^{-2}] is much larger than that typical of Class I protostars, while the *K*-band magnitude of $\sim$12.2 mag is comparable to the brightness of Class I protostars in the R CrA cloud. Therefore, X_W might be a Class I source seen at a large inclination angle. On the other hand, IRS 7 had been suspected to be the counterpart of an X-ray flare source seen during an *ASCA* observation (Koyama et al. 1996). However, the N_H measured during the *ASCA* flare ($\sim4\times10^{22}$ cm^{-2}) was significantly smaller than that of X_W, even considering that the *ASCA* spectrum is contaminated by emission from surrounding Class I protostars with lower N_H. If the *ASCA* flare source is really X_W, the absorption column must be variable.

7. SUMMARY AND CONCLUSION

We discovered two extremely embedded X-ray sources at the positions of the strong VLA centimeter radio sources in the IRS 7 star-forming core. Thanks to its vicinity to the Sun ($d \sim 170$ pc), the large effective area of *XMM-Newton* and an opportunity to catch an active phase, we obtained around $\sim$2000 photons from X_E, which is about 40 times better than the other extremely embedded X-ray sources observed so far. The upper limit to the *K*-band luminosity was restricted to $\sim$1/150 of the extremely embedded protostars in the OMC-2/3 cloud ($d \sim 450$ pc and completeness limit $\sim$16 mag; Tsujimoto et al. 2003). This is therefore a rare, high signal-to-noise ratio X-ray detection of what appears to be a Class 0 protostar or a protostar in an intermediate phase between Class 0 and Class I. The combination of *XMM-Newton* and *Chandra* observations enabled us to study the X-ray emission mechanism in detail. The source showed a significant long-term X-ray variation by a factor of 10–100. The X-ray properties, $kT \sim 3\text{–}4$ keV and $\log L_X \sim 31$ ergs s^{-1}, are comparable to magnetically active X-ray flaring sources, although the light curve of X_E does not suggest flaring activity. These results may suggest that the X-ray activity was enhanced by mass accretion. The X-ray flux during $\mathrm{Obs}_{XMM\,2}$ increased monotonically by a factor of 2 in 30 ks, and the X-ray spectra showed a strong iron fluorescent line with an EW of 250–800 eV. These phenomena may be related to the partial blocking of the X-ray plasma, or perhaps they are indicative of rotation of a hot spot on the protostellar core.

The evolutionary status of X_E should be constrained by constructing the IR and radio SED. This requires high spatial resolution and high sensitivity. *Spitzer*, the Atacama Large Millimeter Array (ALMA), and 8 m class ground-based telescopes are well suited to examine this mysterious X-ray protostar. On the other hand, long-exposure X-ray observations would confirm the fluorescent line profile and test the suggested periodicity in the X-ray brightness. These studies would help us to understand the physical nature of protostars at the earliest phase.

We are grateful to M. Choi, T. Hunter, T. Yokoyama, K. Tatematsu, M. Tsujimoto, H. Murakami, K. Koyama, S. Yashiro, Y. Tsuboi, and the anonymous referee for useful comments. This work was performed while K. H. held awards by National Research Council Research Associateship Award at NASA/GSFC, and is supported by *XMM-Newton* US grant.

REFERENCES

Anderson, I. M., Harju, J., Knee, L. B. G., & Haikala, L. K. 1997, A&A, 321, 575
André, P., Ward-Thompson, D., & Barsony, M. 1993, ApJ, 406, 122
Aschenbach, B., Briel, U. G., Haberl, F., Bräuninger, H. W., Burkert, W., Oppitz, A., Gondoin, P., & Lumb, D. H. 2000, Proc. SPIE, 4012, 731
Brown, A. 1987, ApJ, 322, L31
Chini, R., et al. 2003, A&A, 409, 235
Choi, M., & Tatematsu, K. 2004, ApJ, 600, L55
Favata, F., Giardino, G., Micela, G., Sciortino, S., & Damiani, F. 2003, A&A, 403, 187
Favata, F., Micela, G., Baliunas, S. L., Schmitt, J. H. M. M., Güdel, M., Harnden, F. R., Sciortino, S., & Stern, R. A. 2004, A&A, 418, L13
Feigelson, E. D., Carkner, L., & Wilking, B. A. 1998, ApJ, 494, L215
Garmire, G., & Garmire, A. 2002, APS Meeting Abstracts, 17064
Grosso, N., Montmerle, T., Feigelson, E. D., André, P., Casanova, S., & Gregorio-Hetem, J. 1997, Nature, 387, 56
Güdel, M., et al. 2001, in The Future of Cool-Star Astrophysics, ed. A. Brown, G. M. Harper, & T. R. Ayres (Boulder: Univ. Colorado Press), 303
Hamaguchi, K., Corcoran, M. F., & Imanishi, K. 2003, PASJ, 55, 981
Harju, J., Haikala, L. K., Mattila, K., Mauersberger, R., Booth, R. S., & Nordh, H. L. 1993, A&A, 278, 569
Harju, J., Higdon, J. L., Lehtinen, K., & Juvela, M. 2001, in ASP Conf. Ser. 235, Science with the Atacama Large Millimeter Array, ed. A. Wootten (San Francisco: ASP), 125
Henning, T., Launhardt, R., Steinacker, J., & Thamm, E. 1994, A&A, 291, 546
Imanishi, K., Koyama, K., & Tsuboi, Y. 2001, ApJ, 557, 747
Inoue, H. 1985, Space Sci. Rev., 40, 317
Jansen, F., et al. 2001, A&A, 365, L1
Kastner, J. H., Huenemoerder, D. P., Schulz, N. S., Canizares, C. R., & Weintraub, D. A. 2002, ApJ, 567, 434
Kastner, J. H., et al. 2004, Nature, 430, 429
Knude, J., & Høg, E. 1998, A&A, 338, 897
Koyama, K., Hamaguchi, K., Ueno, S., Kobayashi, N., & Feigelson, E. D. 1996, PASJ, 48, L87
Marti, J., Rodriguez, L. F., & Reipurth, B. 1995, ApJ, 449, 184
McClintock, J. E., & Remillard, R. A. 2005, in Compact Stellar X-Ray Sources, ed. W. H. G. Lewin & M. van der Klis (Cambridge: Cambridge Univ. Press), in press (astro-ph/0306213)

Mewe, R., Kaastra, J. S., & Liedahl, D. A. 1995, Legacy, 6, 16
Montmerle, T., Grosso, N., Tsuboi, Y., & Koyama, K. 2000, ApJ, 532, 1097
Morrison, R., & McCammon, D. 1983, ApJ, 270, 119
Pravdo, S. H., Feigelson, E. D., Garmire, G., Maeda, Y., Tsuboi, Y., & Bally, J. 2001, Nature, 413, 708
Rho, J., Ramírez, S. V., Corcoran, M. F., Hamaguchi, K., & Lefloch, B. 2004, ApJ, 607, 904
Saraceno, P., André, P., Ceccarelli, C., Griffin, M., & Molinari, S. 1996, A&A, 309, 827
Shibata, K., & Yokoyama, T. 2002, ApJ, 577, 422
Skinner, S., Gagné, M., & Belzer, E. 2003, ApJ, 598, 375
Stelzer, B., Neuhäuser, R., & Hambaryan, V. 2000, A&A, 356, 949
Stern, R. A. 1998, in ASP Conf. Ser. 154, Cool Stars, Stellar Systems, and the Sun, ed. R. A. Donahue & J. A. Bookbinder (San Francisco: ASP), 223
Strüder, L., et al. 2001, A&A, 365, L18
Townsley, L. K., Broos, P. S., Garmire, G. P., & Nousek, J. A. 2000, ApJ, 534, L139
Tsuboi, Y., Imanishi, K., Koyama, K., Grosso, N., & Montmerle, T. 2000, ApJ, 532, 1089
Tsuboi, Y., Koyama, K., Hamaguchi, K., Tatematsu, K., Sekimoto, Y., Bally, J., & Reipurth, B. 2001, ApJ, 554, 734
Tsuboi, Y., Koyama, K., Murakami, H., Hayashi, M., Skinner, S., & Ueno, S. 1998, ApJ, 503, 894
Tsujimoto, M., Koyama, K., Kobayashi, N., Goto, M., Tsuboi, Y., & Tokunaga, A. T. 2003, AJ, 125, 1537
Tsujimoto, M., Koyama, K., Kobayashi, N., Saito, M., Tsuboi, Y., & Chandler, C. J. 2004, PASJ, 56, 341
Turner, M. J. L., et al. 2001, A&A, 365, L27
Ueda, Y., et al. 1998, Nature, 391, 866
van den Ancker, M. E. 1999, Ph.D. thesis, Univ. Amsterdam
Weisskopf, M. C., Brinkman, B., Canizares, C., Garmire, G., Murray, S., & Van Speybroeck, L. P. 2002, PASP, 114, 1
Wilking, B. A., McCaughrean, M. J., Burton, M. G., Giblin, T., Rayner, J. T., & Zinnecker, H. 1997, AJ, 114, 2029 (W97)